Realizing Majorana Kramers pairs in two-channel InAs-Al nanowires with highly misaligned electric fields

Benjamin D. Woods and Mark Friesen
Department of Physics, University of Wisconsin-Madison, Madison, Wisconsin 53706, USA

(Received 20 April 2023; revised 12 October 2023; accepted 13 October 2023; published 24 October 2023)

Common proposals for realizing topological superconductivity and Majorana zero modes in semiconductor-superconductor hybrids require large magnetic fields, which paradoxically suppress the superconducting gap of the parent superconductor. Although two-channel schemes have been proposed as a way to eliminate magnetic fields, geometric constraints make their implementation challenging, since the channels should be immersed in nearly antiparallel electric fields. Here, we propose an experimentally favorable scheme for realizing field-free topological superconductivity, in two-channel InAs-Al nanowires, that overcomes such growth constraints. Crucially, we show that antiparallel fields are not required, if the channels are energetically detuned. We compute topological phase diagrams for realistically modeled nanowires, finding a broad range of parameters that could potentially harbor Majorana zero modes. This paper, therefore, solves a major technical challenge and opens the door to near-term experiments.

DOI: 10.1103/PhysRevB.108.155142

I. INTRODUCTION

Majorana zero modes (MZMs) are zero-energy modes localized at the ends of topological superconductors and a potential building block for topological qubits [1–4]. Over the past decade, there has been considerable progress in realizing MZMs in semiconductor-superconductor hybrids [5–12], primarily in the context of the Lutchyn-Oreg model [13,14], which requires applying a large magnetic field to the hybrid system. The application of magnetic fields is worrisome, however, since it suppresses the superconductivity [15,16]. This has motivated research into topological superconductivity in the absence of magnetic fields, so-called time-reversal invariant topological superconductivity (TRITSC) [17–35], where the MZMs on either end of a wire occur in pairs called Majorana Kramers pairs (MKP), due to the preservation of time-reversal symmetry. Of particular interest are proposals that rely on two channels with approximately opposite spin-orbit coupling vectors, such as Rashba bilayers [18–20] and two-channel nanowires [24–28], where the system is essentially composed of two copies of the Lutchyn-Oreg model with the spin degree of freedom replaced by the channel degree of freedom.

The planar geometry of Rashba bilayers naturally provides antiparallel spin-orbit vectors in the two channels, as illustrated in Fig. 1(a), because the spin-orbit vectors align with the local electric field. Creating such structures in semiconductor-superconductor hybrids is challenging, however, because it requires growing a high-quality semiconducting crystal layer between two superconductors, which has yet to be demonstrated. In contrast, epitaxial growth of superconductors on semiconductor nanowires has already been accomplished [36]. In this case, however, it is difficult to engineer antiparallel spin-orbit vectors in the two channels. This is a serious problem because small misalignments of the spin-orbit vectors are expected to collapse the topological gap [24], by effectively coupling the two copies of the Lutchyn-Oreg model present in the wire.

In this paper, we turn the problem on its head by showing that TRITSC can be realized in experimentally feasible [37,38] two-channel hybrid nanowires *where the spin-orbit vectors of the two channels are highly misaligned*, as depicted in Fig. 1(b). The key to our proposal is to introduce an energy detuning between the two channels, on order of the superconducting gap. Essentially, the detuning separates the two copies of the Lutchyn-Oreg model in momentum space, which significantly reduces the coupling induced by the spin-orbit vector misalignment, allowing the topological phase to persist. Since the success of our proposal hinges on the degree of spin-orbit vector misalignment and other device parameters, we consider a more rigorous device model than the Hamiltonian-level models typically used in the literature, incorporating both geometric and electrostatic details. This ensures that our conclusions do not result from inaccurate estimates of the model parameters.

II. MODEL

We consider the system shown in Fig. 1(c) in which a semiconducting InAs nanowire with a triangular cross section is coupled to two Al superconductors that cover half of the upper facets. The system is translationally invariant along the $\hat{z}$ axis. Similar to previous TRITSC proposals [24–27], an external flux loop [39] imposes an order parameter phase difference of π between the two superconductors. In addition, gates surround the nanowire to control the electrostatics. The system is modeled by a Bogoliubov-de-Gennes (BdG) Hamiltonian of the canonical form [40,41]

$$H_{\mathrm{BdG}}(k_z) = \begin{pmatrix} H_N(k_z) & \widetilde{\Delta} \\ -\widetilde{\Delta}^* & -H_N^*(-k_z) \end{pmatrix}, \tag{1}$$

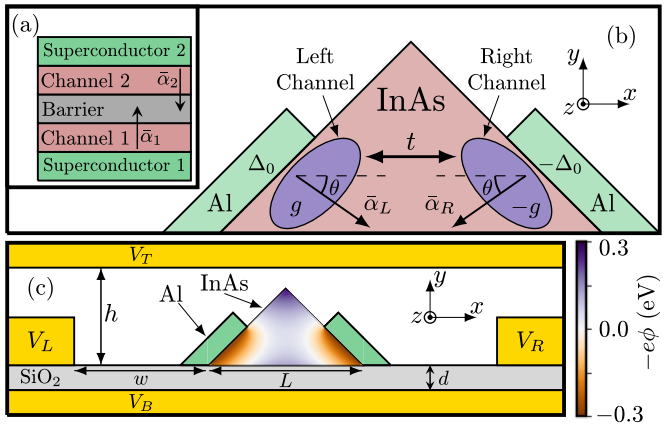

FIG. 1. Structures for realizing TRITSC. (a) Schematic cross section of a proposed Rashba bilayer system, where two superconductors are coupled to two tunnel-coupled channels, with opposite spin-orbit vectors, $\bar{\boldsymbol{\alpha}}_2 = -\bar{\boldsymbol{\alpha}}_1$. Here, the spin-orbit vectors align to the local electric field produced by charge inside of the channels. (b) Schematic cross section of the InAs-Al hybrid nanowire system proposed here, where two channels (blue ovals) with highly misaligned spin-orbit vectors, $\bar{\boldsymbol{\alpha}}_L$ and $\bar{\boldsymbol{\alpha}}_R$, form near the InAs-Al interfaces. Various parameters appearing in the low-energy effective Hamiltonian, Eq. (4), are labeled, including the tunnel coupling t, energy detuning g, spin-orbit misalignment angle θ, and superconductive pairing $\pm\Delta_0$. (c) Zoomed-out view (not drawn to scale) of the system in (b), showing the gates (gold) used to control the electrostatic environment. The potential $-e\phi$ calculated for the gate voltages $(V_T, V_B, V_L, V_R) = (-5.5, -3, 0, 0)$ V and the InAs-Al interface boundary condition $\phi = 0.3$ V is plotted in the cross section of the nanowire.

where H_N and $\widetilde{\Delta}$ are the normal and superconductive pairing components, respectively, k_z is the momentum along the $\hat{z}$ axis, and the first and second columns act upon particle and hole degrees of freedom, respectively. The normal Hamiltonian takes the form $H_N = H_0 + H_{\mathrm{SO}}$, where H_0 is an effective mass Hamiltonian given by

$$H_0(k_z) = \frac{\hbar^2}{2m^*}\left(-\partial_x^2 - \partial_y^2 + k_z^2\right) - e\phi(x, y). \tag{2}$$

Here, m^* is the effective mass and ϕ is the electrostatic potential that satisfies Poisson's equation, $\boldsymbol{\nabla} \cdot [\epsilon(\mathbf{r})\boldsymbol{\nabla}\phi(\mathbf{r})] = -\rho(\mathbf{r})$, where ϵ is a material-dependent dielectric constant and ρ is the free-charge density that is calculated self-consistently [42]. The potential ϕ satisfies Dirichlet boundary conditions on the gates shown in Fig. 1(c). The surfaces of the Al superconductors are also set to $\phi = 0$, except for the InAs-Al interfaces, which are set to $\phi = 0.3$ V to account for the band offset between the two materials [43–46]. The spin-orbit term H_{SO} is given by

$$H_{\mathrm{SO}}(k_z) = [\widetilde{\alpha}_x(x, y)\sigma_y - \widetilde{\alpha}_y(x, y)\sigma_x]k_z, \tag{3}$$

where $\widetilde{\alpha}_j$ are Rashba fields and σ_j are Pauli spin matrices. We neglect Dresselhaus and transverse-Rashba spin-orbit coupling contributions because they are weak, as explained in Appendix D. Importantly, the Rashba fields are position dependent and related to the potential by $\widetilde{\boldsymbol{\alpha}}(x, y) = eC\boldsymbol{\nabla}\phi(x, y)$ [47,48], where C is a material-dependent constant. Finally, the superconductive pairing is treated as an induced pairing within the InAs, with $\widetilde{\Delta} = i\Delta(x, y)\sigma_y$. (See details below.)

A. Two-channel effective Hamiltonian

We derive the low-energy effective Hamiltonian of the system by considering the electrostatic potential shown in Fig. 1(c), for typical gate voltages. Here, electrons are attracted to the InAs-Al interfaces, primarily because of the band offset between the materials, and we observe channels forming near each InAs-Al interface, as illustrated in Fig. 1(b). We then project Eq. (1) onto the two lowest-energy orbital subbands, φ_1 and φ_2, defined by $H_0(0)\varphi_n(x, y) = \varepsilon_n\varphi_n(x, y)$, where φ_1 and φ_2 can be expressed as superpositions of the left and right channel wave functions, χ_L and χ_R, depicted in Fig. 1(b), $\varphi_n = a_n\chi_L + b_n\chi_R$ for $n = 1, 2$. In this two-channel basis, as shown in Appendix A, the effective BdG Hamiltonian becomes

$$\begin{aligned} H_{\mathrm{eff}}(k_z) = {} & [\varepsilon(k_z)\lambda_0 + t\lambda_x + g\lambda_z]\sigma_0\tau_z - \Delta_0\sigma_y\lambda_z\tau_y \\ & + \alpha k_z(\cos\theta\sigma_y\lambda_z\tau_z + \sin\theta\sigma_x\lambda_0\tau_0), \end{aligned} \tag{4}$$

where σ_j, λ_j, and τ_j are Pauli matrices acting on spin, channel, and particle-hole space, respectively, and $\varepsilon(k_z) = \hbar^2k_z^2/(2m^*) - \mu$ is the bare dispersion. By defining $h_{ij} = \langle\chi_i|H_0(0)|\chi_j\rangle$, we can express the chemical potential as $\mu = (h_{LL}+h_{RR})/2$, the interchannel tunnel coupling as $t = h_{RL}$, and the channel energy detuning as $g = (h_{LL}-h_{RR})/2$. We note that these parameters all depend on the local electrostatics. For example, t characterizes the localization of the channels near the InAs-Al interfaces, while g is largely determined by the voltage bias $V_L - V_R$ between the side gates, shown in Fig. 1(c). To understand the parameters α and θ in Eq. (4), it is helpful to define the spin-orbit vector of channel i as $\bar{\boldsymbol{\alpha}}_i = \int |\chi_i(x, y)|^2\widetilde{\boldsymbol{\alpha}}(x, y)\,dxdy$, which averages the electric field over the channel wave function. The parameters α and θ appearing in Eq. (4) represent the magnitude and direction of the spin-orbit vectors, as illustrated in Fig. 1(b). Crucially, the sample geometry ensures that $\bar{\boldsymbol{\alpha}}_L$ and $\bar{\boldsymbol{\alpha}}_R$ are generically misaligned. Additionally, the symmetry of the nanowire cross section imparts approximate mirror symmetry to the two spin-orbit vectors, such that $\bar{\boldsymbol{\alpha}}_L \cdot \hat{x} \approx -\bar{\boldsymbol{\alpha}}_R \cdot \hat{x}$ and $\bar{\boldsymbol{\alpha}}_L \cdot \hat{y} \approx \bar{\boldsymbol{\alpha}}_R \cdot \hat{y}$. This is reflected in the λ_z and λ_0 factors in the second line of Eq. (4). The angle θ characterizes the misalignment between the spin-orbit vectors, and how far the system is from the *ideal limit* ($\theta = 0$), typically assumed in the literature [18–20,25–28]. In a real device, the spin-orbit vectors will not be perfectly mirror symmetric, due to the voltage bias $V_L - V_R$ and device imperfections. We neglect such symmetry-breaking terms here for simplicity, and because they do not significantly affect the physics, as shown in Appendix A. Finally, we note that the superconductive pairing for channel i could also be computed as $\Delta_i = \int |\chi_i(x, y)|^2\Delta(x, y)\,dxdy$, in principle. However, a rigorous calculation of $\Delta(x, y)$ involves complicating factors, such as details about disorder and the InAs-Al interface [49], which are beyond the scope of this paper. Here, we simply define $(\Delta_L, \Delta_R) = (\Delta_0, -\Delta_0)$, which captures the π phase difference between the superconducting order parameters, and we adopt a typical value of $\Delta_0 = 0.2$ meV for such InAs-Al hybrids [9].

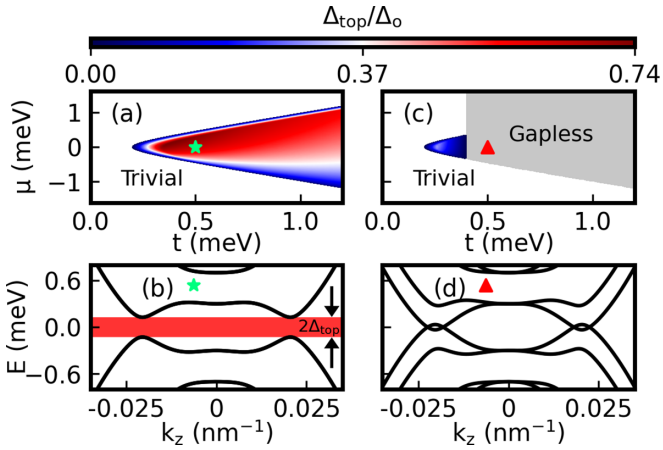

FIG. 2. Topological phase diagrams in the absence of channel detuning. (a) Topological phase diagram for antiparallel spin-orbit vectors ($\theta = 0$) and no channel detuning ($g = 0$). The color map shows the computed topological gap Δ_{top} for the topological phase. (b) Bulk energy spectrum for parameters corresponding to the green star in (a). All bands are twofold degenerate because Eq. (5) decomposes into two identical spin blocks when $\theta = g = 0$. The shaded energy gap corresponds to $2\Delta_{\text{top}}$. (c) Phase diagram for the same system as (a), but with spin-orbit misalignment $\theta = 30^\circ$, yielding a large gapless region (gray). (d) A typical gapless bulk spectrum, for parameters corresponding to the red triangle in (c).

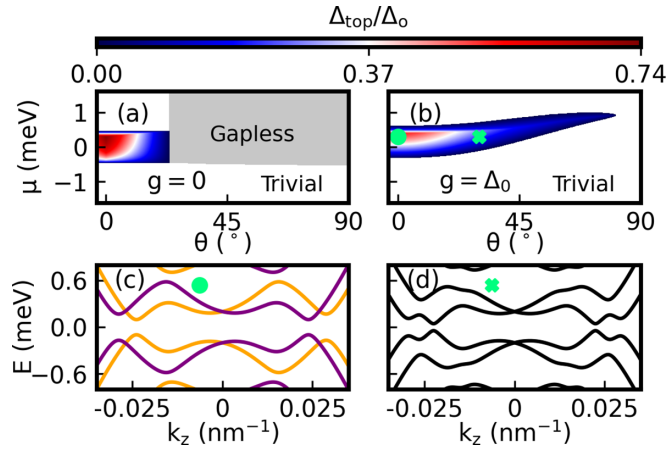

FIG. 3. Effect of channel detuning g on topological phase diagrams. [(a), (b)] Topological phase diagrams, as function of the chemical potential μ and spin-orbit misalignment θ, for $t = 0.5$ meV, and (a) $g = 0$, or (b) $g = \Delta_0$. Increasing θ in (a) suppresses the topological gap Δ_{top}, yielding a gapless phase (gray) when $\theta \gtrsim 22^\circ$. Introducing the channel detuning g in (b) removes the gapless phase and extends the topological region out to large θ. [(c), (d)] Bulk spectra for parameters corresponding to the green circle ($\theta = 0$) and green cross ($\theta = 30^\circ$) in (b). In (c), the channel detuning g lifts the spin degeneracy when $k_z \neq 0$, as shown with orange (purple) for the spin $\uparrow$ ($\downarrow$) bands. Lifting the degeneracy reduces the level repulsion between spins, caused by misaligned spin-orbit vectors, and allows the topological phase to survive up to large θ.

III. TOPOLOGICAL PHASE DIAGRAMS

Before focusing on the device shown in Fig. 1(c), we first explore how the channel degree of freedom enables the realization of TRITSC. Additionally, we show how misalignment of the spin-orbit vector ($\theta \neq 0$) is detrimental to the topological phase and how introducing a channel detuning ($g \neq 0$) can alleviate this issue. For now, the parameters μ, t, g, and θ in Eq. (4) are treated as free parameters, to elucidate the physics of the effective model. However, they are calculated more realistically, later in the paper. Other parameters used here are $m^* = 0.026 m_0$ and $\alpha = 20$ meV nm [9].

To begin, it is helpful to change the basis of the effective Hamiltonian, Eq. (4), as explained in Appendix B, yielding

$$\begin{aligned} H'_{\text{eff}}(k_z) = &[\varepsilon(k_z)\lambda_0\tau_z + t\lambda_x\tau_z - \Delta_0\lambda_y\tau_y \\ &+ \alpha k_z \cos\theta\lambda_z\tau_0]\sigma_0 + g\sigma_z\lambda_z\tau_0 \\ &+ \alpha k_z \sin\theta\sigma_x\lambda_x\tau_0. \end{aligned} \tag{5}$$

We first consider the limit of antiparallel spin-orbit vectors ($\theta = 0$), as typically assumed in the literature [25–28], with no channel detuning ($g = 0$). Equation (5) then decomposes into two identical spin blocks. [This is the reason for the basis change in Eq. (5).] As noted previously [24], each of the spin blocks corresponds to an independent Lutchyn-Oreg model [13,14] of a superconducting nanowire with spin-orbit coupling in an external magnetic field, except that the spin degrees of freedom are now replaced by channels $\sigma_j \to \lambda_j$, and the Zeeman energy is replaced by the interchannel tunnel coupling t. In analogy with the Lutchyn-Oreg model, the system transitions from a trivial phase without MZMs to a topological phase with MZMs when $t^2 > \mu^2 + \Delta_0^2$. In contrast to the Lutchyn-Oreg model, however, *two MZMs (corresponding to one MKP)appear at each end of the nanowire*, due to the presence of dual spin blocks in the TRITSC case. (Note that the degeneracy of the two pairs of MZMs at zero energy is protected by time-reversal symmetry [17].) An example phase diagram is shown in Fig. 2(a) for the case of $\theta = g = 0$. (See Appendix C for a discussion of our method for calculating phase diagrams, which involves determining whether an MKP exists at the end of a semi-infinite wire.)Like other MZM schemes, several device parameters (including the chemical potential) must be tuned simultaneously, to enter the topological phase. Indeed, the range of the chemical potentials yielding a topological phase in Fig. 2(a) is the same range found for Majorana nanowires with broken time-reversal symmetry [13,14]. In Fig. 2(a), the color map indicates the size of the topological gap Δ_{top}, defined by the red region in Fig. 2(b), where we plot a typical bulk energy spectrum. We note that this spectrum is everywhere twofold degenerate, due to the identical spin blocks.

Next, we consider the case of misaligned spin-orbit vectors ($\theta \neq 0$), although we still assume $g = 0$. The term $\alpha k_z \sin\theta\sigma_x\lambda_x\tau_0$ in Eq. (5) now plays an important role, coupling the two spin blocks. This has a dramatic effect on the phase diagram, as shown in Fig. 2(c) for $\theta = 30^\circ$. Here, the topological phase *boundary* is unchanged at small t; however, the topological *gap* is significantly reduced, disappearing all together for large enough t. Importantly, the closing of the gap destroys the topological phase and accompanying MZMs because a topological phase is only well defined in the presence of a bulk gap [50]. This explains why misaligned spin-orbit vectors are considered dangerous for TRITSC [24].

A typical gapless bulk spectrum is shown in Fig. 2(d). Here, the coupling between the spin blocks, due to spin-orbit vector misalignment, causes the degenerate bands to split, when $k_z \neq 0$.

The key result of this paper is that the topological gap can remain robust, even for highly misaligned spin-orbit vectors, if we introduce an energy detuning g between the two channels. This is demonstrated in Figs. 3(a) and 3(b), where we report topological phase diagrams for different channel detunings, as a function of the spin-orbit misalignment angle θ and chemical potential μ. For the case $g = 0$ [Fig. 3(a)], we see that increasing θ suppresses the topological gap, until the system becomes gapless for $\theta \gtrsim 22^\circ$, as consistent with Fig. 2(c). In stark contrast for $g = \Delta_0$ [Fig. 3(b)], there is no gapless phase, and the topological phase remains intact for a range of chemical potentials that is nearly constant for θ between 0 and 40°. In fact, the topological phase extends nearly to the *worst-case limit* of $\theta = 90^\circ$, where the spin-orbit vectors of the two channels are parallel. Detuning is therefore found to be crucial for maintaining a topological phase in TRITSC when $\theta \neq 0$.

To understand the mechanism providing robustness to the topological gap, we first consider the case of $\theta = 0$ and $g \neq 0$. Solving for the gap-closing condition, we obtain the topological criterion, $t^2 > (\mu - E_g)^2 + \Delta_0^2$, where $E_g = \hbar^2 g^2/(2m^*\alpha^2)$. Interestingly, we find that the bulk gap does not close at $k_z = 0$, as in the Lutchyn-Oreg model, but rather at $k_z = \mp g/\alpha$. More importantly, the topological criterion is the same as the $g = 0$ case, except for an overall shift to larger chemical potentials. Therefore, introducing the channel detuning g by itself does not alter the size of the topological region. We then consider the spectrum for $\theta = 0$ and $g = \Delta_0$, in the topological regime [Fig. 3(c)]. Comparing this to the $g = 0$ spectrum in Fig. 2(b), we see that the channel detuning g breaks the twofold spin degeneracy when $k_z \neq 0$. This occurs because the $g\sigma_z\lambda_z\tau_0$ term in Eq. (5) renders the two spin blocks inequivalent. If we also misalign the spin-orbit vectors ($\theta \neq 0$), as shown in Fig. 3(d) for the case $\theta = 30^\circ$, we find that the topological gap is reduced, as expected from Fig. 2. However, the topological gap is more robust, because the band minima are separated in k_z space [see Fig. 3(c)], effectively reducing the level repulsion between the two spin blocks when $\theta \neq 0$. Finally, we note that, to be effective, g must be comparable to other energies in the problem, which are of order of the induced gap Δ_0.

IV. FULL DEVICE CALCULATIONS

We now compute topological phase diagrams for the device shown in Fig. 1(c), as well as the parameters t, θ, and α appearing in the effective Hamiltonian, Eq. (5). The results suggest that prospects for realizing TRITSC in such a device are very promising, and validate the conclusions of Figs. 2 and 3 in a realistic setting. For these calculations, we adopt the geometric parameters $(L, d, h, w) = (65, 50, 90, 100)$ nm and assume a 45° angle at the base of the nanowire, as consistent with recent experiments [38]. The triangular cross section is found to be beneficial for TRITSC by providing single-subband occupancy in the conduction band, while maintaining a large interchannel tunnel coupling t, due to the large surface-to-volume ratio. As before, the band offset at the InAs-Al interfaces is set to 0.3 V [51], and other parameters are given by $C = 1.17\,\mathrm{nm}^2$ and $(\epsilon_{\mathrm{InAs}}, \epsilon_{\mathrm{SiO_2}}) = (14.6, 3.9)$ [52]. Our numerical procedure begins by self-consistently [42] solving the Schrödinger-Poisson equations, treating the charge density in the Hartree approximation. Here, the orbital subbands φ_n of H_0 in Eq. (2) are solved using finite-element methods [53] and the electrostatic potential is solved with help from the FEniCS software library [54]. Note that we focus on the very-low-density regime, where self-consistency has only a modest impact on the results. We then use the solutions obtained for φ_n to calculate the matrix elements of H_{SO} and $\widetilde{\Delta}$. Projecting onto just a few ($n \lesssim 10$) low-energy subbands, we finally calculate the local density of states near zero energy, for a semi-infinite wire, as described in Appendices A and C. This procedure is repeated for a range of system parameters to obtain a topological phase diagram.

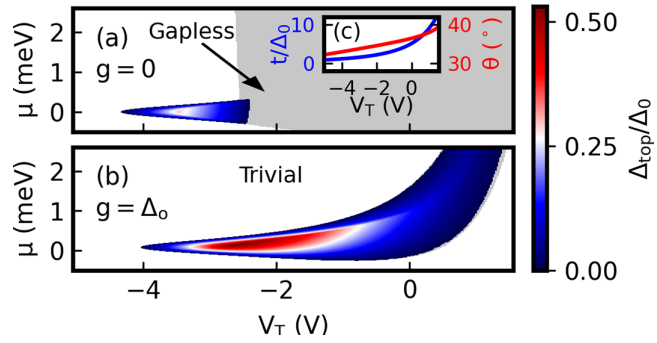

FIG. 4. Topological phase diagrams for full device. Phase diagrams are shown for the device in Fig. 1(c), as functions of top gate voltage V_T and chemical potential μ, for channel detuning values of (a) $g = 0$, or (b) $g = \Delta_0$. Similar to Figs. 3(a) and 3(b), we find a large gapless region (gray) in (a) for $g = 0$, which is nearly removed in (b) by introducing a channel detuning $g = \Delta_0$. (Inset) Normalized tunnel coupling t/Δ_0 (blue) and spin-orbit misalignment angle θ (red), which characterize the effective Hamiltonian in Eq. (4), and are numerically extracted as a function of top gate voltage V_T, for $\mu = g = 0$. Note that the width of the topological region, as a function of μ, is largely determined by t. Also note that $\theta \approx 35^\circ$ for all V_T, indicating highly misaligned spin-orbit vectors. Parameters like t and θ depend strongly on the device geometry and electrostatics.

Figures 4(a) and 4(b) compare the topological phase diagrams obtained for the different channel detuning values, (a) $g = 0$ and (b) $g = \Delta_0$. Here, the back gate and top gate provide full control over the chemical potential μ, where $\mu = 0$ is defined as the Fermi energy lying halfway between the first two subband energies, at $k_z = 0$. The phase diagrams can be understood in analogy to Figs. 2 and 3. In short, Fig. 4(a) shows a large gapless region, due to the absence of channel detuning ($g = 0$). However, this region almost disappears in 4(b), when we include a channel detuning $g = \Delta_0$ by applying a voltage bias $V_L - V_R$. The striking difference between Figs. 4(a) and 4(b) can be attributed to the channel detuning in the presence of highly misaligned spin-orbit vectors. Here, the computed misalignment angle θ is shown in the inset (red curve), and is found to range from 32° to 39°, remaining close to 45° due to the geometry. The topological gap in Fig. 4(b) is also large, indicating a robust topological phase. Moreover,

the phase diagram is quite broad with respect to μ, particularly for larger V_T values, due to the exponential dependence of the interchannel tunnel coupling t on V_T, as shown in the inset (blue curve). We note that a broad phase diagram is particularly conducive for forming MZMs, since larger fluctuations in μ can be tolerated along the length of the wire, without admitting localized Andreev bound states [55–63]. Finally, we obtain a spin-orbit magnitude of $\alpha \approx 25$ meV nm for the range of voltages shown in Fig. 4, a spin-orbit energy of $E_{\mathrm{SO}} = m^*\alpha^2/(2\hbar^2) \approx 0.11$ meV, and a spin-orbit length of $l_{\mathrm{SO}} = \hbar^2/(m^*\alpha) \approx 115$ nm. This large spin-orbit coupling arises mainly from the electric field induced by the band offset at the InAs-Al interfaces.

V. CONCLUSIONS

Contrary to previous expectations [24], we have shown how TRITSC may be realized in InAs-Al two-channel nanowires with highly misaligned spin-orbit vectors. The key ingredient in our scheme is an energy detuning g between the two channels. By incorporating geometrical and electrostatic details into a realistic device model, we have shown that MZMs can be realized, without magnetic fields, using currently existing InAs-Al technology [37,38].

We caution, however, that the proposed scheme still requires a high degree of uniformity along the length of the wire to avoid forming low-energy Andreev bound states, similar to other MZM schemes. Moreover, fluctuations of the interchannel tunnel coupling t and the detuning parameter g could also affect the formation of Andreev bound states, in addition to more well-studied fluctuations of the chemical potential μcoming from electrostatic nonuniformities [55–60], including smooth confinement potentials at the edges of the wire [61–63]. Finally, we note that the decoupling of the MKP in TRITSC relies upon time-reversal symmetry. Magnetic impurities, such as Overhauser fields from nuclear spins, familiar to the quantum dot community [64], could therefore be detrimental and will be addressed in future work.

ACKNOWLEDGMENTS

We are grateful to M. A. Eriksson and T. D. Stanescu for helpful discussions. This research was sponsored in part by the Army Research Office (ARO) under Award No. W911NF-22-1-0090, and by the National Science Foundation (NSF) through QLCI-HQAN (Award No. 2016136). The views, conclusions, and recommendations contained in this document are those of the authors and are not necessarily endorsed nor should they be interpreted as representing the official policies, either expressed or implied, of the Army Research Office (ARO) or the U.S. Government. The U.S. Government is authorized to reproduce and distribute reprints for Government purposes notwithstanding any copyright notation herein.

APPENDIX A: DERIVATION OF THE TWO-CHANNEL EFFECTIVE HAMILTONIAN

In the main text, we stated that the effective Hamiltonian H_{eff} in Eq. (4) can be derived by projecting the BdG Hamiltonian H_{BdG} in Eq. (1) onto the two-channel orbital wave functions χ_L and χ_R, which are superpositions of the two lowest-energy orbital subbands φ_1 and φ_2 of the effective mass Hamiltonian H_0. In this section, we provide details regarding this derivation. For clarity, some statements from the main text will be repeated here.

To begin, we define an orbital subband φ_n as the eigenstate of the effective mass Hamiltonian H_0 for $k_z = 0$, i.e.,

$$H_0(0)\varphi_n(x,y) = \varepsilon_n\varphi_n(x,y), \tag{A1}$$

where ε_n is the subband energy and $n \in \mathbb{N}^+$. Note that $\varphi_n(x,y)$ can be chosen to be real valued, which we adopt. Also note that the orbital subband φ_n is only an orbital wave function, which does not contain spin. This is well defined because the effective mass Hamiltonian H_0 is spin independent, i.e., H_0 is proportional to the identity operator σ_0 in spin space. We can construct a subband wave function with spin using a simple tensor product, $\varphi_{n,\sigma} = \varphi_n(x,y)\,|\sigma\rangle$, where $\sigma = \uparrow, \downarrow$. Furthermore, we can define a BdG subband wave function that specifies both the spin and particle-hole degrees of freedom as the tensor product, $\varphi_{n,\sigma,\tau} = \varphi_n(x,y)\,|\sigma\,\tau\rangle$, where $\tau = p$ for particle and $\tau = h$ for hole.

We now rewrite our BdG Hamiltonian using the basis consisting of the BdG subband wave functions $\{\varphi_{n,\sigma,\tau}\}$. This leads to the BdG Hamiltonian

$$H'_{BdG}(k_z) = \begin{pmatrix} H'_N(k_z) & \widetilde{\Delta}' \\ -\widetilde{\Delta}'^{*} & -H'^{*}_N(-k_z) \end{pmatrix}, \tag{A2}$$

where $H'_N(k_z)$ and $\widetilde{\Delta}'$ are matrices whose elements are found by evaluating the expressions, $\langle\varphi_{m,\sigma}|H_N(k_z)|\varphi_{n,\sigma'}\rangle$ and $\langle\varphi_{m,\sigma}|\widetilde{\Delta}|\varphi_{n,\sigma'}\rangle$, respectively. Performing these calculations, we find $H'_N(k_z)$ and $\widetilde{\Delta}'$ can be expressed as

$$H'_N(k_z) = \bar{\Lambda}(k_z)\sigma_0 + \bar{\alpha}_x k_z\sigma_y - \bar{\alpha}_y k_z\sigma_x, \tag{A3}$$

$$\widetilde{\Delta}' = i\bar{\Delta}\sigma_y, \tag{A4}$$

where σ_j are Pauli spin matrices. Here, $\bar{\Lambda}$, $\bar{\alpha}_x$, $\bar{\alpha}_y$, and $\bar{\Delta}$ are real-symmetric matrices with elements,

$$\bar{\Lambda}_{mn}(k_z) = \delta_{mn}\left(\varepsilon_n + \frac{\hbar^2 k_z^2}{2m^*}\right), \tag{A5}$$

$$(\bar{\alpha}_j)_{mn} = eC\int \varphi_m(x,y)(\partial_j\phi)\varphi_n(x,y)\,dxdy, \tag{A6}$$

$$\bar{\Delta}_{mn} = \int \varphi_m(x,y)\Delta(x,y)\varphi_n(x,y)\,dxdy. \tag{A7}$$

Notice that $\bar{\Lambda}$ is diagonal in subband space since the kinetic energy term $\hbar^2k_z^2/(2m^*)$ in the effective mass Hamiltonian $H_0(k_z)$ has no spatial dependence. The spin-orbit $\bar{\alpha}_j$ and superconductive pairing $\bar{\Delta}$ matrices, in contrast, couple different subbands because of the spatial inhomogeneity of $\phi(x,y)$ and $\Delta(x,y)$. The full BdG Hamiltonian $H'_{\mathrm{BdG}}(k_z)$ can then be expressed as

$$H'_{\mathrm{BdG}}(k_z) = \bar{\Lambda}(k_z)\sigma_0\tau_z + \bar{\alpha}_x k_z\sigma_y\tau_z - \bar{\alpha}_y k_z\sigma_x\tau_0 - \bar{\Delta}\sigma_y\tau_y, \tag{A8}$$

where τ_j are Pauli matrices acting in particle-hole space.

The largest energy scale present in Eq. (A8) is the energy separation between most subbands, i.e., $\varepsilon_m - \varepsilon_n$ for $m \neq n$. In comparison, the $\bar{\alpha}_j$ and $\bar{\Delta}$ terms that provide inter-subband

coupling are small perturbations. We can then arrive at a low-energy effective Hamiltonian that captures all of the relevant low-energy physics by projecting $H'_{\mathrm{BdG}}(k_z)$ onto a few low-energy subbands. As stated in the main text, the two lowest-energy subbands φ_1 and φ_2 are superpositions of the left and right channel wave functions χ_L and χ_R, depicted in Fig. 1(b) of the main text: $\varphi_n = a_n\chi_L + b_n\chi_R$ for $n = 1, 2$. The channel wave functions, being strongly localized near the InAs-Al interfaces as shown in Fig. 1(b) of the main text, have relatively weak tunnel coupling $t = \langle\chi_R|H_0(0)|\chi_L\rangle$, which leads to a small subband energy difference $\varepsilon_2 - \varepsilon_1 \approx 2t$ between the two lowest-energy subbands. Indeed, t is typically on the same energy scale as $\bar{\alpha}_j k_z$ and $\bar{\Delta}$. We, therefore, need to keep both φ_1 and φ_2 in the low-energy basis to capture the relevant low-energy physics. In contrast, $\varepsilon_3 - \varepsilon_2 \gg \varepsilon_2 - \varepsilon_1$ since $\varepsilon_3 - \varepsilon_2 \sim \hbar^2/(m^*\ell^2)$, where ℓ is the small length scale associated with the localization of the channel wave functions near each InAs-Al interface. Therefore, the relevant low-energy physics can be fully captured while ignoring subbands φ_n for $n \geqslant 3$. In other words, we only keep the first two rows and columns of the $\bar{\Lambda}$, $\bar{\alpha}_x$, $\bar{\alpha}_y$, and $\bar{\Delta}$ matrices in Eq. (A8) for our low-energy effective Hamiltonian.

Finally, we transform the low-energy effective Hamiltonian from the basis containing the first two orbital subbands φ_1 and φ_2 to the basis containing the two channels χ_L and χ_R. To do so, we explicitly define the channel wave functions as

$$\begin{pmatrix}\chi_L(x,y)\\ \chi_R(x,y)\end{pmatrix} = O\begin{pmatrix}\varphi_1(x,y)\\ \varphi_2(x,y)\end{pmatrix}, \tag{A9}$$

where O is an orthogonal matrix. Specifically, we choose O such that the channel wave functions are maximally separated from one another in the x direction, i.e., $\Delta x = \langle\chi_R|x|\chi_R\rangle - \langle\chi_L|x|\chi_L\rangle$ is maximized. To find such an O, we first define X as

$$X = \begin{pmatrix}\langle\varphi_1|x|\varphi_1\rangle & \langle\varphi_1|x|\varphi_2\rangle\\ \langle\varphi_2|x|\varphi_1\rangle & \langle\varphi_2|x|\varphi_2\rangle\end{pmatrix}, \tag{A10}$$

i.e., the matrix representation of the x operator within the subspace containing the two lowest-energy orbital subbands. Δx is then maximized by choosing O to be the matrix which diagonalizes X, $O^T X O = \mathrm{diag}(\widetilde{x}_1, \widetilde{x}_2)$ where $\widetilde{x}_1 < \widetilde{x}_2$. An example is shown in Fig. 5 of the wave functions of the two lowest-energy orbital subbands, φ_1 and φ_2, and how they decompose into left and right channel wave functions, χ_L and χ_R. Note that in the case where we have mirror symmetry about the $\hat{y}$ axis ($g = 0$), the channel wave functions, χ_L and χ_R, are simply the even and odd equal superpositions of the orbital subband wave functions, φ_1 and φ_2, as is the case in Fig. 5. Evaluating the effective BdG Hamiltonian in this new basis, where the channel wave functions χ_L and χ_R replace the orbital subbands φ_1 and φ_2, then yields the two-channel effective Hamiltonian,

$$\begin{aligned}H^{\mathrm{eff}}_{BdG}(k_z) =& \left[\left(\frac{\hbar^2 k_z^2}{2m^*} - \mu\right)\lambda_0 + t\lambda_x + g\lambda_z\right]\sigma_0\tau_z - \Delta_0\sigma_y\lambda_z\tau_y\\ &+ \alpha k_z(\cos\theta\sigma_y\lambda_z\tau_z + \sin\theta\sigma_x\lambda_0\tau_0)\\ &+ (\eta_1\lambda_0 + \xi_1\lambda_x)k_z\sigma_y\tau_z + (\eta_2\lambda_z + \xi_2\lambda_x)k_z\sigma_x\tau_0\\ &+ (\Delta_1\lambda_0 + \Delta_2\lambda_x)\sigma_y\tau_y,\end{aligned} \tag{A11}$$

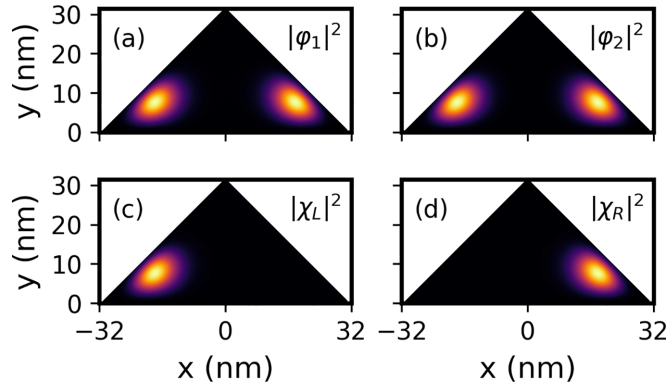

FIG. 5. Wave function profiles for the two lowest-energy orbital subbands φ_1 and φ_2 are shown in (a) and (b), respectively. These subbands can be decomposed into left and right channels whose wave functions χ_1 and χ_2 are shown in (c) and (d), respectively. Note that these channel wave functions are localized near the InAs-Al interfaces because of the strong band bending near these interfaces, which is primarily due to the band offset between the materials. The gate voltages for this calculation are $V_T = -5.5\,\mathrm{V}$, $V_B = -3\,\mathrm{V}$, $V_L = V_R = 0$, and the boundary condition at the InAs-Al interfaces is $\phi = 0.3\,\mathrm{V}$. Note that the electrostatic potential $\phi(x, y)$ within the InAs nanowire for these gate settings is shown in Fig. 1(c) of the main text.

where σ_j, λ_j, and τ_j with $j = 0, x, y, z$ are Pauli matrices acting in spin, channel, and particle-hole space, respectively. In other words, the first and second columns of a λ_j matrix correspond to the left and right channel, respectively. The parameters in Eq. (A11) are given by the expressions,

$$\mu = (h_{LL} + h_{RR})/2, \tag{A12}$$

$$t = h_{RL}, \tag{A13}$$

$$g = (h_{LL} - h_{RR})/2, \tag{A14}$$

$$\Delta_0 = (d_{LL} - d_{RR})/2, \tag{A15}$$

$$\alpha\cos\theta = \left(s^x_{LL} - s^x_{RR}\right)/2, \tag{A16}$$

$$\alpha\sin\theta = -\left(s^y_{LL} + s^y_{RR}\right)/2, \tag{A17}$$

$$\eta_1 = \left(s^x_{LL} + s^x_{RR}\right)/2, \tag{A18}$$

$$\eta_2 = -\left(s^y_{LL} - s^y_{RR}\right)/2, \tag{A19}$$

$$\xi_1 = s^x_{RL}, \tag{A20}$$

$$\xi_2 = -s^y_{RL}, \tag{A21}$$

$$\Delta_1 = (d_{LL} + d_{RR})/2, \tag{A22}$$

$$\Delta_2 = d_{RL}, \tag{A23}$$

where $h_{ij} = \langle\chi_i|H_0(k_z)|\chi_j\rangle$, $s^x_{ij} = \langle\chi_i|\widetilde{\alpha}_x(x,y)|\chi_j\rangle$, $s^y_{ij} = \langle\chi_i|\widetilde{\alpha}_y(x,y)|\chi_j\rangle$, and $d_{ij} = \langle\chi_i|\Delta(x,y)|\chi_j\rangle$ with $i, j = L, R$. Note that Eq. (A11) contains additional terms involving η_1, η_2, ξ_1, ξ_2, Δ_1, and Δ_2 that are not show in Eq. (4) of the

main text. Here, η_1 and η_2 account for the fact that the x and y components of the electric field at the positions of the two channels are only *approximately* opposite and equal, respectively. The terms ξ_1 and ξ_2 account for the interchannel spin-orbit coupling, as indicated by the λ_x matrix. The Δ_1 and Δ_2 terms allow for differences between the two channels in pairing strength and interchannel pairing, respectively. These six terms in our calculations are all found to be small and do not qualitatively impact the physics of the effective model. For simplicity, we have ignored these terms when showing the effective Hamiltonian in Eq. (4) of the main text. However, these terms have been included in the calculation of the topological phase diagrams shown in Figs. 4(a) and 4(b) of the main text. Furthermore, we find that ignoring these terms only slightly changes the phase diagrams with no qualitative differences.

APPENDIX B: TRANSFORMATION OF THE TWO-CHANNEL EFFECTIVE HAMILTONIAN

In the main text, we stated that the two-channel effective Hamiltonian $H_{\text{eff}}(k_z)$ shown in Eq. (4) transforms into $H'_{\text{eff}}(k_z)$ shown in Eq. (5). The Hamiltonians are connected by the relation $H'_{\text{eff}}(k_z) = U^\dagger H_{\text{eff}}(k_z) U$, where U is a unitary matrix. Here, we provide the form of U and discuss its structure. The goal of the transformation is to bring the Hamiltonian into a form where the spins are decoupled for the ideal limit of antiparallel spin-orbit vectors ($\theta = 0$).

The unitary matrix U is best understood as the product of four simple transformations, $U = R_x^\sigma S_h^\sigma S_h^\lambda S_\downarrow^\lambda$, where R and S stand for rotation and swap operations that we now explain. The first operation R_x^σ is a rotation of the spins by 90° about the x axis,

$$R_x^\sigma = \frac{1}{\sqrt{2}}(1 + i\sigma_x\tau_z). \tag{B1}$$

This results in the transformed Hamiltonian $H_1(k_z) = R_x^{\sigma\,\dagger} H_{\text{eff}}(k_z) R_x^\sigma$ given by

$$\begin{aligned} H_1(k_z) = &[\varepsilon(k_z)\lambda_0 + t\lambda_x + g\lambda_z]\sigma_0\tau_z - \Delta_0\sigma_y\lambda_z\tau_y \\ &+ \alpha k_z(\cos\theta\sigma_z\lambda_z\tau_o + \sin\theta\sigma_x\lambda_0\tau_0), \end{aligned} \tag{B2}$$

where we see that the spin-orbit coupling aligns with the z axis for the ideal limit of antiparallel spin-orbit vectors ($\theta = 0$). Next, we notice that the superconductive pairing exists between particles and holes of the opposite spin species, as evident in the $\Delta_0\sigma_y\lambda_z\tau_y$ term. We want, however, the pairing to exist between the same spin species since we are seeking a final Hamiltonian that is block diagonal in spin space for the case of $\theta = 0$. To accomplish this, we swap the spin degrees of freedom in the hole sector using the operator,

$$S_h^\sigma = \tfrac{1}{2}[\sigma_0(\tau_0 + \tau_z) + \sigma_x(\tau_0 - \tau_z)]. \tag{B3}$$

This results in the transformed Hamiltonian $H_2(k_z) = S_h^{\sigma\,\dagger} H_1(k_z) S_h^\sigma$ given by

$$\begin{aligned} H_2(k_z) = &[\varepsilon(k_z)\lambda_0 + t\lambda_x + g\lambda_z]\sigma_0\tau_z + \Delta_0\sigma_z\lambda_z\tau_x \\ &+ \alpha k_z(\cos\theta\sigma_z\lambda_z\tau_z + \sin\theta\sigma_x\lambda_0\tau_0), \end{aligned} \tag{B4}$$

where we see that the Hamiltonian is indeed block diagonal in spin space for the case of $\theta = 0$. Next, we notice that the superconductive pairing within each spin block is diagonal in channel space. We want, however, the channels to play the role of ordinary spins in an s-wave superconductor, which have superconductive pairing between particles and holes of *opposite* spin. In order to make the channel degree of freedom better resemble the ordinary spin degree of freedom, we swap the channel degrees of freedom in the hole sector using the operator,

$$S_h^\lambda = \tfrac{1}{2}[\lambda_0(\tau_0 + \tau_z) + \lambda_x(\tau_0 - \tau_z)]. \tag{B5}$$

This results in the transformed Hamiltonian $H_3(k_z) = S_h^{\lambda\,\dagger} H_2(k_z) S_h^\lambda$ given by

$$\begin{aligned} H_3(k_z) = &[\varepsilon(k_z)\lambda_0 + t\lambda_x]\sigma_0\tau_z + g\sigma_0\lambda_z\tau_0 - \Delta_0\sigma_z\lambda_y\tau_y \\ &+ \alpha k_z(\cos\theta\sigma_z\lambda_z\tau_o + \sin\theta\sigma_x\lambda_0\tau_0). \end{aligned} \tag{B6}$$

Interestingly for $g = 0$, each diagonal spin block of Eq. (B6) is exactly the Lutchyn-Oreg Hamiltonian of Refs. [13,14] for a superconducting nanowire with spin-orbit coupling in an external magnetic field, except that the spin degrees of freedom are replaced by channels $\sigma_j \to \lambda_j$, and the Zeeman energy is replaced by the interchannel tunnel coupling t. The diagonal spin blocks are not identical, however, since they have opposite superconductive pairing and spin-orbit coupling coefficients, as evident by the σ_z in the $\Delta_0\sigma_z\lambda_y\tau_y$ and $\alpha k_z \cos\theta\sigma_z\lambda_z\tau_o$ terms. The spin blocks become identical if we swap the channel degrees of freedom within the spin $\downarrow$ sector using the operator,

$$S_\downarrow^\lambda = \tfrac{1}{2}[(\sigma_0 + \sigma_z)\lambda_0 + (\sigma_0 - \sigma_z)\lambda_x]. \tag{B7}$$

Finally, this results in the effective Hamiltonian $H'_{\text{eff}}(k_z) = S_h^{\lambda\,\dagger} H_3(k_z) S_h^\lambda = U^\dagger H_{\text{eff}}(k_z) U$ shown in Eq. (5) of the main text. Notice that this last operation transforms the $g\sigma_0\lambda_z\tau_o$ term in $H_3(k_z)$ into $g\sigma_z\lambda_z\tau_o$, where the channel detuning g is effectively opposite for the two spin blocks. As stressed in the main text, this difference between the spin blocks arising from the channel detuning g is responsible for the increased robustness of the topological phase to spin-orbit vector misalignment ($\theta = 0$). Lastly, we note that the product of these four simple operations can be algebraically manipulated into the more compact expression,

$$U = \tfrac{1}{4}(1 + i[\sigma_x + \sigma_y + \sigma_z])(1 - i\sigma_z\lambda_x)(1 + i\lambda_x\tau_z). \tag{B8}$$

APPENDIX C: PHASE DIAGRAM CALCULATION METHOD

In the main text, we provide several phase diagrams showing the boundary between the trivial and topological phases, as well as the topological gap Δ_{top} within the topological regions. Often times, the assignment of trivial and topological phases is done by calculating a topological invariant [41]. In this paper, we use an alternative technique where we look for the presence of zero-energy Majorana zero modes at the end of a semi-infinite system. To do so, we first discretize the Hamiltonian in Eq. (A11) on a 1D lattice with a small lattice spacing of $a = 0.5$ nm. Note that each site of the 1D lattice has eight orbitals to account for the spin, channel, and particle-hole degrees of freedom. Information about the local density of states is then contained in the Green's function

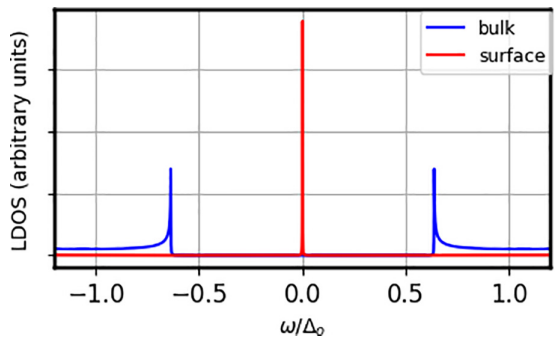

FIG. 6. Surface (red) and bulk (blue) local density of states for a system in the topological phase. The presence of Majorana zero modes is evident from the peak in the surface local density of states at zero energy $\omega = 0$. The absence or presence of such a peak can be used to determine if the system is in the trivial or topological phase for any given choice of parameters. System parameters are $m^* = 0.026m_o$, $\Delta_0 = 0.2\,\text{meV}$, $t = 0.5\,\text{meV}$, $\alpha = 20\,\text{meV nm}$, and $\theta = 0$. All other parameters in Eq. (A11) are zero.

matrix $G(\omega) = (\omega I - H_{dis} + i\eta)^{-1}$, where $\omega \in \mathbb{R}$ is the input energy, H_{dis} is the discretized Hamiltonian matrix, I is the identity matrix, and $\eta = 10^{-5}\,\text{meV}$ is a small energy to bring the Green's function into the upper half of the complex plane. While generic matrix inversion is numerically expensive, finding the diagonal elements of $G(\omega)$ can be done in a numerically efficient manner for systems with translation invariance by using the decimation technique of Ref. [65]. Using this technique, the surface Green's function block G_s (which is just the block of the Green's function matrix for the first lattice site) and the bulk Green's function block G_b can be found for a system with 2^N lattice sites using only N decimation iterations. These, in turn, give us the surface and bulk local density of states,

$$LDOS_s(\omega) = -\frac{1}{\pi}\text{Im}(\text{Tr}[G_s(\omega)]), \tag{C1}$$

$$LDOS_b(\omega) = -\frac{1}{\pi}\text{Im}(\text{Tr}[G_b(\omega)]). \tag{C2}$$

Using $N = 50$ iterations, we can then obtain the surface and bulk density of states for system of length $L \approx 10^6\,\text{m}$, which is semi-infinite for all practical purposes. An example of the surface and bulk local density of states for a system in the topological phase is shown in Fig. 6. We see a peak in the surface local density of states at zero energy $\omega = 0$ coming from the presence of Majorana zero modes at the ends of the system. The absence or presence of such a peak can then be used to determine if the system is in the trivial or topological phase for any given choice of parameters. In addition, we can read off the topological gap Δ_{top} of the topological phase from the location of the coherence peaks in the bulk local density of states (blue curve in Fig. 6).

APPENDIX D: QUANTIFYING DRESSELHAUS AND TRANSVERSE-RASHBA SPIN-ORBIT COUPLING

In the main text, we only included Rashba spin-orbit coupling and limited it to the component involving the longitudinal momentum k_z [see Eq. (3) of main text]. However, there also exists Rashba spin-orbit coupling involving the transverse momenta k_x and k_y, along with Dresselhaus spin-orbit coupling. Within in the main text, we neglected these terms due to their contributions yielding only small quantitative effects while not affecting the qualitative aspects of the physics. In this Appendix, we quantify these other forms of spin-orbit coupling to show that neglecting them is well justified.

Let us begin with the Dresselhaus spin-orbit coupling, which arises from the bulk inversion asymmetry of the InAs zinc blende lattice. Its Hamiltonian component, which is to be added to H_{SO} in Eq. (3) of the main text, takes the form [52]

$$H_{\text{BIA}} = \gamma_D\big[\big(k_y^2 - k_z^2\big)k_x\sigma_x + \big(k_z^2 - k_x^2\big)k_y\sigma_y + \big(k_x^2 - k_y^2\big)k_z\sigma_z\big], \tag{D1}$$

where γ_D is a material-dependent constant given by $\gamma_D = 27.18\,\text{meV nm}^3$ for InAs [52]. (Reference [66] gives a similar value of $\gamma_D = 21.7\,\text{meV nm}^3$.) Note that the Dresselhaus spin-orbit Hamiltonian takes the particular form shown in Eq. (D1) because the triangular InAs nanowires studied in this work are grown along the [001] crystallographic direction with the upper facets of the nanowire being within the [110] and $[\bar{1}10]$ planes [47]. Otherwise, the appropriate coordinate rotation would have to be applied to Eq. (D1). Projecting the Dresselhaus Hamiltonian onto the two-channel basis defined in Appendix A leads to the term

$$H_{\text{BdG}}^{\text{eff,BIA}} = \nu_x\sigma_x\lambda_y\tau_0 + \nu_y\sigma_y\lambda_y\tau_z + \left[\left(\frac{\beta_{LL} + \beta_{RR}}{2}\right)\lambda_0 + \left(\frac{\beta_{LL} - \beta_{RR}}{2}\right)\lambda_z + \beta_{LR}\lambda_x\right]k_z\sigma_z\tau_0 + \mathcal{O}\big(k_z^2\big), \tag{D2}$$

which should be added to $H_{\text{BdG}}^{\text{eff}}$ in Eq. (A11). Here, ν_x and ν_y are interchannel spin-orbit coupling coefficients that come from the two terms in Eq. (D1) not involving the longitudinal momentum k_z and are given by

$$\nu_x = -i\gamma_D\langle\chi_R|k_xk_y^2|\chi_L\rangle, \tag{D3}$$

$$\nu_y = i\gamma_D\langle\chi_R|k_x^2k_y|\chi_L\rangle, \tag{D4}$$

where χ_L and χ_R are the channel wave functions. Note that these terms do not produce analogous *intrachannel* spin-orbit coupling coefficients. This is because the expectation values of the operators $k_xk_y^2$ and $k_x^2k_y$ automatically vanish since they both have an imaginary prefactor when expressed as differential operators and the channel wave functions χ_i are real valued. The β_{ij} coefficients come from the term involving σ_z in Eq. (D1) and are given by

$$\beta_{ij} = \gamma_D\langle\chi_i|k_x^2 - k_y^2|\chi_j\rangle. \tag{D5}$$

Note that both interchannel β_{LR} and intrachannel β_{ii} coefficients exist since the expectation value of the operator $k_x^2 - k_y^2$ for each channel wave function generically does not vanish.

The values of the β_{ij} coefficients are shown in Fig. 7(a) as a function of top gate voltage V_T for $\mu = g = 0$. The interchannel coefficient β_{LR} and intrachannel coefficient β_{ii} are shown as blue (dashed) and gold (solid) lines, respectively. Note that $\beta_{LL} = \beta_{RR}$ because of mirror symmetry about the $\hat{y}$

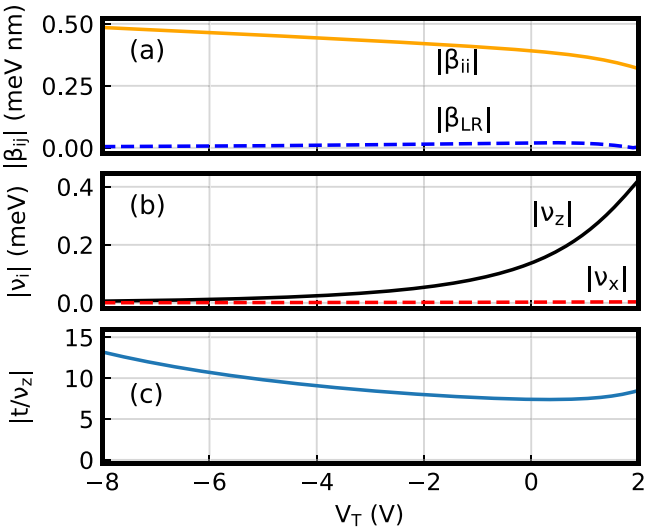

FIG. 7. Spin-orbit coefficients from Dresselhaus and transverse-Rashba spin-orbit coupling as a function of top gate voltage V_T for $\mu = g = 0$. (a) Intrachannel β_{ii} (solid gold) and interchannel β_{LR} Dresselhaus coefficients (dashed blue). The intrachannel Dresselhaus coefficient β_{ii} dominates for the interchannel Dresselhaus coefficient β_{LR}. Furthermore, the intrachannel Dresselhaus coefficient β_{ii} is smaller than the numerically extracted Rashba spin-orbit coefficient of $\alpha \approx 25\,\text{meV}\cdot\text{nm}$ (given in the main text) by over a factor of 40. (b) Interchannel spin-orbit coefficients ν_x and ν_z that come from Dresselhaus and transverse-Rashba spin-orbit coupling, respectively. (c) Ratio of interchannel tunnel coupling t and interchannel spin-orbit coefficient ν_z, showing that the spin-independent coupling t dominates over the spin-dependent coupling ν_z.

axis when $g = 0$. Notice that the interchannel coefficient β_{LR} is smaller than the intrachannel coefficient β_{ii} by at least an order of magnitude over the entire voltage range. Furthermore, comparing the intrachannel Dresselhaus coefficient β_{ii} to the extracted Rashba spin-orbit coefficient of $\alpha \approx 25\,\text{meV nm}$ from the main text, we see that β_{ii} is smaller by over a factor of 40. Therefore, we conclude that the Dresselhaus terms involving β_{ij} have a negligible effect on the physics. In addition, the interchannel spin-orbit coefficient ν_x is shown in Fig. 7(b) as a function of V_T, as a red (dashed) line. We numerically find that ν_x is always small ($\nu_x \lesssim 1\,\mu\text{eV}$), and is therefore safely neglected. Finally, we also numerically found that ν_y from Dresselhaus spin-orbit coupling vanishes, and, therefore, plays no role in our system.

It is interesting to note that the physical reason why the intrachannel coefficients β_{ii} are so small in this system is because the upper facets of the InAs nanowire are within the [110] and [$\bar{1}$10] planes. To understand this, notice first that the left channel wave function χ_L in Fig. 7(c) closely resembles a particle-in-a-box state with quantization axes that are $\approx 45^\circ$ with respect to the x and y axes, respectively, that is, along the [110] and [$\bar{1}$10] crystallographic directions. Next, we can rewrite the $k_x^2 - k_y^2$ operator appearing in Eq. (D5) as

$$k_x^2 - k_y^2 = 2k_{x'}k_{y'}, \tag{D6}$$

where the x' and y' axes align with the [110] and [$\bar{1}$10] crystallographic directions. Importantly, a particle-in-a-box state

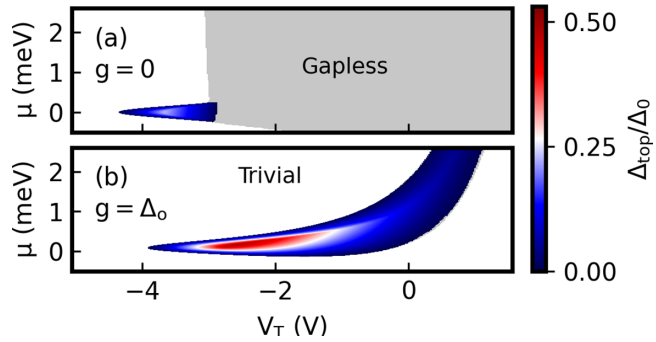

FIG. 8. Topological phase diagram of the same system as Fig. 4 of the main text except that the $\nu_z\sigma_z\lambda_y\tau_0$ term from transverse-Rashba spin-orbit coupling is included in the model. Comparing the results to Figs. 4(a) and 4(b) of the main text, we find that inclusion of the transverse-Rashba spin-orbit coupling slightly reduces the area of the topological phase and the topological gap Δ_{top} within the topological region. The effect is quite modest although.

with quantization axes along the x' and y' axes has vanishing expectation value for the operator $k_{x'}k_{y'}$. This is because the the operators $k_{x'}$ and $k_{y'}$ have imaginary prefactors when expressed as differential operators, and the particle-in-a-box state decomposes into a product of real wave functions in the x' and y' direction. Now, χ_L is not perfectly captured by a product state separable in the x' and y' direction, so β_{LL} does not exactly vanish. Its close resemblance, however, keeps β_{LL} very small.

Next, let us consider the transverse-Rashba spin-orbit coupling. The Rashba spin-orbit coupling included within H_{SO} in Eq. (3) of the main text only involves longitudinal momentum k_z, whereas transverse-Rashba spin-orbit coupling involves the transverse momenta k_x and k_y. Its Hamiltonian component, which is to be added to H_{SO} in Eq. (3) of the main text, is given by [48]

$$\begin{aligned} H_{R_\perp} = \tfrac{1}{2}([\alpha_y(x,y)k_x + k_x\alpha_y(x,y)] \\ - [\alpha_x(x,y)k_y + k_y\alpha_x(x,y)])\sigma_z, \end{aligned} \tag{D7}$$

where care has been taken to properly symmetrize the operators such that the Hamiltonian is Hermitian. Projecting the transverse-Rashba Hamiltonian onto the two-channel basis defined in Appendix A leads to the term

$$H_{\text{BdG}}^{\text{eff},R_\perp} = \nu_z\sigma_z\lambda_y\tau_0, \tag{D8}$$

which should be added to $H_{\text{BdG}}^{\text{eff}}$ in Eq. (A11). Here, ν_z is an interchannel spin-orbit coupling coefficient given by

$$\begin{aligned} \nu_z = \frac{i}{2}\langle\chi_R|(\alpha_y(x,y)k_x + k_x\alpha_y(x,y))|\chi_L\rangle \\ - \frac{i}{2}\langle\chi_R|(\alpha_x(x,y)k_y + k_y\alpha_x(x,y))|\chi_L\rangle. \end{aligned} \tag{D9}$$

Note that the transverse-Rashba Hamiltonian does not produce an analogous *intrachannel* spin-orbit coupling coefficient. This is because the expectation values of the operators k_x and k_y automatically vanish for the same reason given above for the $k_xk_y^2$ and $k_x^2k_y$ operators.

The interchannel spin-orbit coefficient ν_z is shown in Fig. 7(b) as a function of V_T, as a black (solid) line. We find

that the interchannel spin-orbit coefficient ν_z coming from transverse-Rashba spin-orbit coupling is comparable to the superconducting gap $\Delta_0 = 0.2\,\text{meV}$ for the larger top gate voltages in Fig. 7(b). It may then at first seem we cannot ignore the transverse-Rashba spin-orbit coupling. However, if we compare this coupling to the interchannel coupling t, as shown in Fig. 7(c), we see that ν_z is smaller by roughly an order of magnitude within the entire voltage range. We therefore do not expect ν_z to play a significant role in the physics of the system. To test this expectation, we redo the calculation of the topological phase diagrams shown in Figs. 4(a) and 4(b) of the main text with the inclusion of the $\nu_z\sigma_z\lambda_y\tau_0$ term into the effective two-channel Hamiltonian given in Eq. (A11). The results are shown in Fig. 8, again for two values of channel detuning, (a) $g = 0$ and (b) $g = \Delta_0$. Comparing the results to Figs. 4(a) and 4(b) of the main text, we see that the addition of transverse-Rashba spin-orbit coupling has a modest effect on the topological phase diagrams. The results are qualitatively the same as the results in Figs. 4(a) and 4(b) of the main text, with the only quantitative differences being a small reduction of the topological region and the reduction of the topological gap Δ_{top} within the topological region. Therefore, we conclude that while transverse-Rashba spin-orbit coupling is slightly detrimental to topological superconductivity in our system, the effect is quite small and does not qualitatively impact the physics.

[1] S. B. Bravyi and A. Y. Kitaev, Fermionic quantum computation, Ann. Phys. **298**, 210 (2002).

[2] C. Nayak, S. H. Simon, A. Stern, M. Freedman, and S. Das Sarma, Non-Abelian anyons and topological quantum computation, Rev. Mod. Phys. **80**, 1083 (2008).

[3] J. Alicea, New directions in the pursuit of Majorana fermions in solid state systems, Rep. Prog. Phys. **75**, 076501 (2012).

[4] V. Lahtinen and J. K. Pachos, A short introduction to topological quantum computation, SciPost Phys. **3**, 021 (2017).

[5] V. Mourik, K. Zuo, S. M. Frolov, S. R. Plissard, E. P. A. M. Bakkers, and L. P. Kouwenhoven, Signatures of Majorana fermions in hybrid superconductor-semiconductor nanowire devices, Science **336**, 1003 (2012).

[6] M. T. Deng, C. L. Yu, G. Y. Huang, M. Larsson, P. Caroff, and H. Q. Xu, Anomalous zero-bias conductance peak in a Nb-InSb nanowire-Nb hybrid device, Nano Lett. **12**, 6414 (2012).

[7] J. Chen, P. Yu, J. Stenger, M. Hocevar, D. Car, S. R. Plissard, E. P. A. M. Bakkers, T. D. Stanescu, and S. M. Frolov, Experimental phase diagram of zero-bias conductance peaks in superconductor/semiconductor nanowire devices, Sci. Adv. **3**, e1701476 (2017).

[8] H. J. Suominen, M. Kjaergaard, A. R. Hamilton, J. Shabani, C. J. Palmstrøm, C. M. Marcus, and F. Nichele, Zero-energy modes from coalescing Andreev states in a two-dimensional semiconductor-superconductor hybrid platform, Phys. Rev. Lett. **119**, 176805 (2017).

[9] R. M. Lutchyn, E. P. A. M. Bakkers, L. P. Kouwenhoven, P. Krogstrup, C. M. Marcus, and Y. Oreg, Majorana zero modes in superconductor-semiconductor heterostructures, Nat. Rev. Mater. **3**, 52 (2018).

[10] H. Zhang, M. W. A. de Moor, J. D. S. Bommer, D. Xu, G. Wang, N. van Loo, C.-X. Liu, S. Gazibegovic, J. A. Logan, D. Car *et al.*, Large zero-bias peaks in InSb-Al hybrid semiconductor-superconductor nanowire devices, arXiv:2101.11456

[11] M. Aghaee, A. Akkala, Z. Alam, R. Ali, A. Alcaraz Ramirez, M. Andrzejczuk, A. E. Antipov, P. Aseev, M. Astafev, B. Bauer, J. Becker, S. Boddapati, F. Boekhout, J. Bommer, T. Bosma, L. Bourdet, S. Boutin, P. Caroff, L. Casparis, M. Cassidy *et al.*, InAs-Al hybrid devices passing the topological gap protocol, Phys. Rev. B **107**, 245423 (2023).

[12] S. D. Sarma, In search of Majorana, Nat. Phys. **19**, 165 (2023).

[13] R. M. Lutchyn, J. D. Sau, and S. Das Sarma, Majorana fermions and a topological phase transition in semiconductor-superconductor heterostructures, Phys. Rev. Lett. **105**, 077001 (2010).

[14] Y. Oreg, G. Refael, and F. von Oppen, Helical liquids and Majorana bound states in quantum wires, Phys. Rev. Lett. **105**, 177002 (2010).

[15] B. S. Chandrasekhar, A note on the maximum critical field of high-field superconductors, Appl. Phys. Lett. **1**, 7 (1962).

[16] A. M. Clogston, Upper limit for the critical field in hard superconductors, Phys. Rev. Lett. **9**, 266 (1962).

[17] A. Haim and Y. Oreg, Time-reversal-invariant topological superconductivity in one and two dimensions, Phys. Rep. **825**, 1 (2019).

[18] S. Nakosai, Y. Tanaka, and N. Nagaosa, Topological superconductivity in bilayer Rashba system, Phys. Rev. Lett. **108**, 147003 (2012).

[19] Y. Volpez, D. Loss, and J. Klinovaja, Rashba sandwiches with topological superconducting phases, Phys. Rev. B **97**, 195421 (2018).

[20] Y. Volpez, D. Loss, and J. Klinovaja, Second-order topological superconductivity in π-junction Rashba layers, Phys. Rev. Lett. **122**, 126402 (2019).

[21] S. Deng, L. Viola, and G. Ortiz, Majorana modes in time-reversal invariant *s*-wave topological superconductors, Phys. Rev. Lett. **108**, 036803 (2012).

[22] F. Zhang, C. L. Kane, and E. J. Mele, Time-reversal-invariant topological superconductivity and Majorana Kramers pairs, Phys. Rev. Lett. **111**, 056402 (2013).

[23] S. Deng, G. Ortiz, and L. Viola, Multiband *s*-wave topological superconductors: Role of dimensionality and magnetic field response, Phys. Rev. B **87**, 205414 (2013).

[24] A. Keselman, L. Fu, A. Stern, and E. Berg, Inducing time-reversal-invariant topological superconductivity and fermion parity pumping in quantum wires, Phys. Rev. Lett. **111**, 116402 (2013).

[25] E. Gaidamauskas, J. Paaske, and K. Flensberg, Majorana bound states in two-channel time-reversal-symmetric nanowire systems, Phys. Rev. Lett. **112**, 126402 (2014).

[26] C. Schrade, M. Thakurathi, C. Reeg, S. Hoffman, J. Klinovaja, and D. Loss, Low-field topological threshold in Majorana double nanowires, Phys. Rev. B **96**, 035306 (2017).

[27] M. Thakurathi, P. Simon, I. Mandal, J. Klinovaja, and D. Loss, Majorana Kramers pairs in Rashba double nanowires with interactions and disorder, Phys. Rev. B **97**, 045415 (2018).

[28] P. Kotetes, Topological superconductivity in Rashba semiconductors without a Zeeman field, Phys. Rev. B **92**, 014514 (2015).

[29] X.-J. Liu, C. L. M. Wong, and K. T. Law, Non-Abelian Majorana doublets in time-reversal-invariant topological superconductors, Phys. Rev. X **4**, 021018 (2014).

[30] A. Haim, A. Keselman, E. Berg, and Y. Oreg, Time-reversal-invariant topological superconductivity induced by repulsive interactions in quantum wires, Phys. Rev. B **89**, 220504(R) (2014).

[31] J. Klinovaja and D. Loss, Time-reversal invariant parafermions in interacting Rashba nanowires, Phys. Rev. B **90**, 045118 (2014).

[32] A. Haim, K. Wölms, E. Berg, Y. Oreg, and K. Flensberg, Interaction-driven topological superconductivity in one dimension, Phys. Rev. B **94**, 115124 (2016).

[33] H. Ebisu, B. Lu, J. Klinovaja, and Y. Tanaka, Theory of time-reversal topological superconductivity in double Rashba wires: Symmetries of Cooper pairs and Andreev bound states, Prog. Theor. Exp. Phys. **2016**, 083I01 (2016).

[34] F. Parhizgar and A. M. Black-Schaffer, Highly tunable time-reversal-invariant topological superconductivity in topological insulator thin films, Sci. Rep. **7**, 9817 (2017).

[35] D. Oshima, S. Ikegaya, A. P. Schnyder, and Y. Tanaka, Flat-band Majorana bound states in topological Josephson junctions, Phys. Rev. Res. **4**, L022051 (2022).

[36] P. Krogstrup, N. L. B. Ziino, W. Chang, S. M. Albrecht, M. H. Madsen, E. Johnson, J. Nygård, C. M. Marcus, and T. S. Jespersen, Epitaxy of semiconductor-superconductor nanowires, Nat. Mater. **14**, 400 (2015).

[37] S. Vaitiekėnas, A. M. Whiticar, M.-T. Deng, F. Krizek, J. E. Sestoft, C. J. Palmstrøm, S. Marti-Sanchez, J. Arbiol, P. Krogstrup, L. Casparis, and C. M. Marcus, Selective-area-grown semiconductor-superconductor hybrids: A basis for topological networks, Phys. Rev. Lett. **121**, 147701 (2018).

[38] J. S. Lee, S. Choi, M. Pendharkar, D. J. Pennachio, B. Markman, M. Seas, S. Koelling, M. A. Verheijen, L. Casparis, K. D. Petersson, I. Petkovic, V. Schaller, M. J. W. Rodwell, C. M. Marcus, P. Krogstrup, L. P. Kouwenhoven, E. P. A. M. Bakkers, and C. J. Palmstrøm, Selective-area chemical beam epitaxy of in-plane InAs one-dimensional channels grown on InP(001), InP(111)b, and InP(011) surfaces, Phys. Rev. Mater. **3**, 084606 (2019).

[39] A. Fornieri, A. M. Whiticar, F. Setiawan, E. Portolés, A. C. C. Drachmann, A. Keselman, S. Gronin, C. Thomas, T. Wang, R. Kallaher *et al.*, Evidence of topological superconductivity in planar Josephson junctions, Nature (London) **569**, 89 (2019).

[40] J.-X. Zhu, *Bogoliubov-de Gennes Method and its Applications* (Springer, New York, 2016).

[41] C.-K. Chiu, J. C. Y. Teo, A. P. Schnyder, and S. Ryu, Classification of topological quantum matter with symmetries, Rev. Mod. Phys. **88**, 035005 (2016).

[42] B. D. Woods, S. Das Sarma, and T. D. Stanescu, Subband occupation in semiconductor-superconductor nanowires, Phys. Rev. B **101**, 045405 (2020).

[43] A. Vuik, D. Eeltink, A. R. Akhmerov, and M. Wimmer, Effects of the electrostatic environment on the Majorana nanowire devices, New J. Phys. **18**, 033013 (2016).

[44] A. E. Antipov, A. Bargerbos, G. W. Winkler, B. Bauer, E. Rossi, and R. M. Lutchyn, Effects of gate-induced electric fields on semiconductor Majorana nanowires, Phys. Rev. X **8**, 031041 (2018).

[45] A. E. G. Mikkelsen, P. Kotetes, P. Krogstrup, and K. Flensberg, Hybridization at superconductor-semiconductor interfaces, Phys. Rev. X **8**, 031040 (2018).

[46] B. D. Woods, T. D. Stanescu, and S. Das Sarma, Effective theory approach to the Schrödinger-Poisson problem in semiconductor Majorana devices, Phys. Rev. B **98**, 035428 (2018).

[47] P. Wójcik, A. Bertoni, and G. Goldoni, Tuning Rashba spin-orbit coupling in homogeneous semiconductor nanowires, Phys. Rev. B **97**, 165401 (2018).

[48] S. D. Escribano, A. L. Yeyati, and E. Prada, Improved effective equation for the Rashba spin-orbit coupling in semiconductor nanowires, Phys. Rev. Res. **2**, 033264 (2020).

[49] T. D. Stanescu and S. Das Sarma, Proximity-induced superconductivity generated by thin films: Effects of Fermi surface mismatch and disorder in the superconductor, Phys. Rev. B **106**, 085429 (2022).

[50] T. D. Stanescu, *Introduction to Topological Quantum Matter and Quantum Computation* (CRC Press, Boca Raton, FL, 2017).

[51] S. Schuwalow, N. B. M. Schroeter, J. Gukelberger, C. Thomas, V. Strocov, J. Gamble, A. Chikina, M. Caputo, J. Krieger, G. C. Gardner, M. Troyer, G. Aeppli, M. J. Manfra, and P. Krogstrup, Band bending profile and band offset extraction at semiconductor-metal interfaces, arXiv:1910.02735.

[52] R. Winkler, *Spin-Orbit Coupling Effects in Two-Dimensional Electron and Hole Systems* (Springer, New York, 2003).

[53] B. D. Woods, and T. D. Stanescu, Electrostatic effects and topological superconductivity in semiconductor-superconductor-magnetic insulator hybrid wires, Phys. Rev. B **104**, 195433 (2021).

[54] M. Alnaes, J. Blechta, J. Hake, A. Johansson, B. Kehlet, A. Logg, C. Richardson, J. Ring, M. Rognes, and G. Wells, The fenics project version 1.5, Arch. Numer. Softw. **3**, 100 (2015).

[55] J. D. Sau and S. Das Sarma, Density of states of disordered topological superconductor-semiconductor hybrid nanowires, Phys. Rev. B **88**, 064506 (2013).

[56] D. Rainis, L. Trifunovic, J. Klinovaja, and D. Loss, Towards a realistic transport modeling in a superconducting nanowire with Majorana fermions, Phys. Rev. B **87**, 024515 (2013).

[57] H. Pan and S. Das Sarma, Physical mechanisms for zero-bias conductance peaks in Majorana nanowires, Phys. Rev. Res. **2**, 013377 (2020).

[58] E. Prada, P. San-Jose, M. W. A. de Moor, A. Geresdi, E. J. H. Lee, J. Klinovaja, D. Loss, J. Nygård, R. Aguado, and L. P. Kouwenhoven, From Andreev to Majorana bound states in hybrid superconductor-semiconductor nanowires, Nat. Rev. Phys. **2**, 575 (2020).

[59] B. D. Woods, S. Das Sarma, and T. D. Stanescu, Charge-impurity effects in hybrid Majorana nanowires, Phys. Rev. Appl. **16**, 054053 (2021).

[60] C. Zeng, G. Sharma, S. Tewari, and T. Stanescu, Partially separated Majorana modes in a disordered medium, Phys. Rev. B **105**, 205122 (2022).

[61] G. Kells, D. Meidan, and P. W. Brouwer, Near-zero-energy end states in topologically trivial spin-orbit coupled superconducting nanowires with a smooth confinement, Phys. Rev. B **86**, 100503(R) (2012).

[62] T. D. Stanescu and S. Tewari, Robust low-energy Andreev bound states in semiconductor-superconductor structures:

Importance of partial separation of component Majorana bound states, Phys. Rev. B **100**, 155429 (2019).

[63] A. Vuik, B. Nijholt, A. R. Akhmerov, and M. Wimmer, Reproducing topological properties with quasi-Majorana states, SciPost Phys. **7**, 061 (2019).

[64] D. J. Reilly, J. M. Taylor, J. R. Petta, C. M. Marcus, M. P. Hanson, and A. C. Gossard, Suppressing spin qubit dephasing by nuclear state preparation, Science **321**, 817 (2008).

[65] M. P. L. Sancho, J. M. L. Sancho, J. M. L. Sancho, and J. Rubio, Highly convergent schemes for the calculation of bulk and surface Green functions, J. Phys. F **15**, 851 (1985).

[66] M. Gmitra and J. Fabian, First-principles studies of orbital and spin-orbit properties of GaAs, GaSb, InAs, and InSb zinc-blende and Wurtzite semiconductors, Phys. Rev. B **94**, 165202 (2016).